Available online at www.sciencedirect.com
ScienceDirect
Journal of Magnetic Resonance 184 (2007) 130–142
JMR Journal of Magnetic Resonance
www.elsevier.com/locate/jmr

EPR and HYSCORE investigation of the electronic structure of the model complex Mn(imidazole)$_6$: Exploring Mn(II)–imidazole binding using single crystals

Inés García-Rubio [a,*], Alexander Angerhofer [b], Arthur Schweiger [a,†]

[a] *Laboratory of Physical Chemistry, ETH Zurich, CH-8093 Zürich, Switzerland*
[b] *Department of Chemistry, University of Florida, Gainesville, FL 32611-7200, USA*

Received 21 January 2006
Available online 18 October 2006

Abstract

The electronic structure of the Mn(II)-imidazole binding was studied by EPR spectroscopy using the model complex Mn(Im)$_6$ diluted in a single crystal of Zn(Im)$_6$Cl$_2$·4(H$_2$O). The second rank zero-field splitting (ZFS) tensor (D tensor) of the two sites, a and b, present in the crystal was determined by measuring the orientation patterns of the echo-detected EPR spectra in three different planes at 10 K ($D_a = -106$, $D_b = -118$, $E_a = -17$, $E_b = -22 \times 10^{-4}$ cm^{-1}. Euler angles with respect to the crystal habitus: $\alpha_a = 13°$, $\beta_a = 76°$, $\gamma_a = 108.5°$, $\alpha_b = 14°$, $\beta_b = 73.5°$, $\gamma_b = 103.5°$). The contribution of cubic ZFS terms to the spectrum allowed us to determine the orientation of the N–Mn–N directions of the complex as well (Euler angles in the D tensor reference frame $\alpha = 100°$, $\beta = 23°$, $\gamma = 0°$, both centers having the same orientation). The hyperfine interactions with ^{14}N were explored by HYSCORE spectroscopy. The correlation patterns and modulation amplitudes in the 2D experiments were studied for different electron spin transitions and orientations of the crystal. Signals of three different pairs of nitrogens were found. The results were analyzed considering that the N–Mn binding directions are principal directions of the hyperfine and nuclear quadrupole tensor of ^{14}N. All three pairs of nitrogens were found to be almost equivalent with an isotropic contribution of $A_{iso} \approx 3.2$ MHz and an almost axial anisotropic coupling of $2T \approx 1.1$ MHz along the N–Mn bonding direction. The nuclear quadrupole principal values are 1.5 MHz along the bonding direction, −0.6 MHz in the direction perpendicular to the imidazole plane, and −0.9 MHz in the direction perpendicular to both.

Keywords: Mn(II) binding proteins; High-spin systems; HYSCORE; EPR of Mn(II); Hyperfine structure; Mn(II) single crystal

1. Introduction

Even though only found as a trace element in living organisms, Mn has attracted much attention in the past 15–20 years due to its occurrence in the active sites of about a score of different enzymes, with human MnSOD (superoxide dismutase) and the photosynthetic oxygen-evolving complex being perhaps the most prominent ones. Mn can assume a variety of different oxidation states in these enzymes, the most common being Mn(II) and Mn(III). The ligand environment of the metal center allows for the fine-tuning of its redox potential which is critical for its biological function. Apart from enzymes where it is part of the active site, Mn(II) can replace other ions, sometimes without loss of functionality; for example Mg(II), which is vital for the folding and function of many enzymes and nucleic acids [1,2]. Mn(II), which is a paramagnetic ion with five unpaired electrons and spin $S = 5/2$, is therefore a very popular probe for EPR investigations of metal binding sites and ligand interactions (see Reed and Markham [3] for a review). In all biomolecules containing manganese, this transition metal ion is found to be (very often 6-fold) coordinated to protein residues, substrates and water molecules. Among these, the imino nitrogen in the imidazole

* Corresponding author. Fax: +41 44 632 1021.
E-mail address: garciarubio@esr.phys.chem.ethz.ch (I. García-Rubio).
† Deceased on January 4th, 2006.

1090-7807/$ - see front matter © 2006 Elsevier Inc. All rights reserved.
doi:10.1016/j.jmr.2006.09.013

ring of histidine side chains is one of the most common ligands for Mn(II) ions [1].

Analogues or model complexes of the paramagnetic metalloproteins are often more amenable to detailed scrutiny than the proteins themselves, and their EPR characterization can help to evaluate the spin density distribution, providing a structural framework for understanding the changes that take place during protein activity.

Hyperfine interactions between the unpaired electrons of Mn(II) and nuclear spins in the immediate vicinity of the ion provide a means for unequivocal identification of the ligands. They can also supply information about distances, geometry and the electron spin distribution at the active site. However, continuous-wave (cw) EPR signals from Mn(II) complexes are typically too broad to permit detection of hyperfine splittings from weakly coupled nuclei (superhyperfine coupling) which are normally obscured within the linewidth.

Electron nuclear double resonance (ENDOR) and electron spin echo envelope modulation (ESEEM) spectroscopies, on the other hand, have the potential for detecting hyperfine and nuclear quadrupole couplings even in solid-state broadened EPR spectra. In particular, two-dimensional HYSCORE spectroscopy [4] can provide better resolution, which is required when many magnetic nuclei are close to the paramagnetic center.

Unlike for systems with electron spin $S = 1/2$, ESEEM spectra of high-spin systems have not been widely studied. One of the reasons why investigations of such ions are more difficult is that in orientationally disordered systems a large number of spin transitions contribute to the ENDOR or ESEEM spectra, which results in a loss of spectral resolution. Several theoretical/computational approaches have been explored to determine independently the contributions of the different transitions to the ESEEM spectra [5–8], but these methods have not been sufficiently checked against experimental data.

Some studies report on hyperfine interactions of Mn(II) with magnetic nuclei such as ^{31}P, ^{14}N, ^{1}H, ^{15}N or ^{13}C present in residues, nucleotides or substrates of a number of different Mn(II)-containing or Mn(II)-substituted biomolecules where ESEEM or ENDOR were used to probe the structure and conformational changes of the active site [9–19]. Although some signals in the ESEEM spectra of lectins and cytochrome *c* oxidase have been assigned to a coordinating nitrogen of a histidine residue [20–22], little information is available about manganese–imidazole nitrogen interactions.

To examine in detail the binding between manganese and nitrogen, in particular the manganese–histidine superhyperfine interactions, we studied the model complex $Mn(Im)_6$ by means of *Q*-band HYSCORE spectroscopy. To reduce the problem of overlapping transitions, single crystals were used. Prior to the HYSCORE study the cw-like EPR spectra were measured in three rotational planes of a single crystal. This data provided the zero-field splitting (ZFS) parameters and allowed us to locate the molecular axes of the complex with respect to the crystal habitus. Then, by measuring HYSCORE spectra at different magnetic field orientations, the hyperfine and nuclear quadrupole tensors of the six coordinating nitrogens were determined. We present experimental data on Mn–N hyperfine interactions, where the contributions of the different electron spin transitions have been identified and separated. This information can be used to predict and interpret the spectra of disordered systems containing Mn(II) and provides us with a better understanding of the behavior of the nuclear modulation effect in high-spin systems.

2. Theoretical basis

In the high-spin state the d^5 ion Mn^{2+} has a $^6S_{5/2}$ ground state. Additionally, the isotope ^{55}Mn (100% natural abundance) has a nuclear spin $I = 5/2$. The spin Hamiltonian used to describe the CW-EPR spectra consists of several terms accounting for electron and nuclear Zeeman interactions, hyperfine couplings, zero-field splitting and nuclear quadrupole interactions,

$$H = H_{EZ} + H_{HF} + H_{ZFS} + H_{NZ} + H_{NQ}. \quad (1)$$

The specific form of this Hamiltonian is detailed as a function of spin operators

$$\begin{aligned} H = {} & \mu_B g \mathbf{B_0 S} + \mathbf{IAS} + D\left[S_z^2 - \frac{1}{3}S(S+1)\right] + E(S_x^2 - S_y^2) \\ & + \frac{a}{6}\left[S_{x'}^4 + S_{y'}^4 + S_{z'}^4 - \frac{1}{5}S(S+1)(3S^2+3S-1)\right] \\ & + \frac{F}{180}\left[35S_z^4 - 30S(S+1)S_z^2 + 25S_z^2 - 6S(S+1)\right. \\ & \left. + 3S^2(S+1)^2\right]. \end{aligned} \quad (2)$$

The first term describes the electron Zeeman interaction. Since the ground state has zero orbital angular momentum, the *g* tensor can be considered isotropic and very close to the value of the free electron. The hyperfine interaction of the manganese nucleus described by the second term in Eq. (2) is usually also isotropic. The remaining terms describe the zero-field splitting. The third and fourth terms are the second-rank contributions to the zero-field splitting, which are only different from zero for symmetries lower than cubic. *D* and *E* are the axial and rhombic parameters that describe this traceless ZFS tensor (*D* tensor).

In this work the fourth-rank contributions to the zero-field splitting have also to be considered in the description of the spectra. The fifth term in Eq. (2) is the cubic ZFS term and the sixth term describes the corresponding contribution for axial symmetry. Note that in Eq. (2) S_x, S_y and S_z are the spin operators with respect to the symmetry axes of the *D* tensor and $S_{x'}$, $S_{y'}$ and $S_{z'}$ are the spin operators with respect to the cubic axes. The nuclear Zeeman and nuclear quadrupole coupling terms have been omitted in

Eq. (2), they are not relevant for the interpretation of the cw EPR spectra.

When the spin Hamiltonian in Eq. (2) is dominated by the electron Zeeman interaction, the magnetic fields at which the lines in the spectrum are observed can be written in first order as [23–26],

$$\begin{aligned}
\mathrm{B}\left(\left|\pm\frac{5}{2},m_I\right\rangle \leftrightarrow \left|\pm\frac{3}{2},m_I\right\rangle\right) &= B_0 - Am_I \mp 2[D(3\cos^2\theta - 1) \\
&\quad + 3E\sin^2\theta\cos 2\phi] \mp 2a\Omega \mp \frac{1}{6}Fq \\
\mathrm{B}\left(\left|\pm\frac{3}{2},m_I\right\rangle \leftrightarrow \left|\pm\frac{1}{2},m_I\right\rangle\right) &= B_0 - Am_I \mp [D(3\cos^2\theta - 1) \\
&\quad + 3E\sin^2\theta\cos 2\phi] \mp \frac{5}{2}a\Omega \mp \frac{5}{24}Fq \\
\mathrm{B}\left(\left|-\frac{1}{2},m_I\right\rangle \rightarrow \left|\frac{1}{2},m_I\right\rangle\right) &= B_0 - Am_I, \qquad (3)
\end{aligned}$$

where $q = 35\cos^4\theta - 30\cos^2\theta + 3$ and $\Omega = 1 - 5(l^2m^2 + n^2m^2 + l^2n^2)$; θ and ϕ being the polar and azimuthal angles of the magnetic field with respect to the D tensor and l, m, and n are the direction cosines of the magnetic field with respect to the cubic axes.

Consequently, for the EPR spectrum of Mn(II) one expects 30 lines because the five electron-spin multiplets, which differ in energy due to the zero-field splitting, are further split into six hyperfine lines each. Taking Eq. (3) into account, the hyperfine lines will be spread by the same field value. However, the splitting between the five EPR multiplets is modified by the cubic term of the ZFS in the Hamiltonian.

From the HYSCORE spectra the hyperfine and nuclear quadrupole interactions of the six surrounding nitrogen nuclei ($I = 1$) can be extracted. For each nucleus k the static nuclear spin Hamiltonian is given by

$$H_{n,k} = -\mu_n g_n \mathbf{B}_0\mathbf{I}_k + \mathbf{S}\mathbf{A}_k\mathbf{I}_k + \mathbf{I}_k\mathbf{Q}_k\mathbf{I}_k. \qquad (4)$$

If the ZFS terms are small the electron Zeeman interaction dominates the Hamiltonian in Eq. (2). Then, the effect of the ZFS on the nuclear frequencies can be neglected [6] as the electron spin can be considered quantized along the magnetic field direction **u**. The operator **S** in Eq. (4) can be substituted by $\langle\mathbf{S}\rangle = m_S\mathbf{u}$, where m_S is the expected eigenvalue in each electron spin manifold.

If the nuclear Zeeman interaction is the dominant contribution in the nuclear spin Hamiltonian, or the hyperfine tensor is predominantly isotropic, the nuclear frequencies are given in first order by

$$\begin{aligned}
\nu(\mathrm{dq}) &= 2m_S A_{\mathrm{uu}} - 2\nu_{\mathrm{N}} \\
\nu(sq_1) &= m_S A_{\mathrm{uu}} - \nu_{\mathrm{N}} + \frac{3}{2}Q_{\mathrm{uu}} \qquad (5) \\
\nu(sq_2) &= m_S A_{\mathrm{uu}} - \nu_{\mathrm{N}} - \frac{3}{2}Q_{\mathrm{uu}},
\end{aligned}$$

where A_{uu} and Q_{uu} are the hyperfine and nuclear quadrupole coupling constants along the magnetic field and ν_{N} is the Larmor frequency of nitrogen. Note that the hyperfine contribution to the nuclear frequency depends on the electron spin manifold.

The turning angle β of the magnetization produced by a microwave pulse of duration t_p and magnetic field amplitude B_1 also depends on the electron transition excited by the pulse [8],

$$\beta = c_{m_S m_S'}\mu_B g B_1 t_p,$$

where $c_{m_S m_S'}$is $\sqrt{5}, \sqrt{8}$, and 3 for the transitions $|\pm\frac{5}{2}\rangle \leftrightarrow |\pm\frac{3}{2}\rangle$, $|\pm\frac{3}{2}\rangle \leftrightarrow |\pm\frac{1}{2}\rangle$, and $|\frac{1}{2}\rangle \leftrightarrow |-\frac{1}{2}\rangle$, respectively.

3. Results and analysis

Single crystals of hexaimidazole zinc(II)dichloride-tetrahydrate doped with 0.5% Mn(II) were produced as described in Section 6 and their quality was verified by X-ray diffraction. The structure of the complex is displayed in Fig. 1. The central cation (Zn or Mn) in this complex is coordinated to the imino group of three pairs of opposed imidazole rings that are oriented perpendicular to each other, forming an approximately octahedral environment for the Mn(II) ions. According to the crystal structure, layers of hexaimidazole complexes and layers of chloride ions and water molecules alternate in the crystal [27,28].

3.1. FID-detected and echo-detected EPR

The field-swept EPR spectra were recorded via integration of an FID or a two-pulse echo, resulting in absorption spectra. Forbidden transitions usually do not show up in these spectra, because of the low turning angles [29]. An advantage of these techniques over conventional cw-EPR is their ability to show appropriate intensities in spectra with very broad lines. In cw-EPR with field modulation such lines are usually very weak in intensity. The measurements were carried out at Q-band (~35 GHz). At

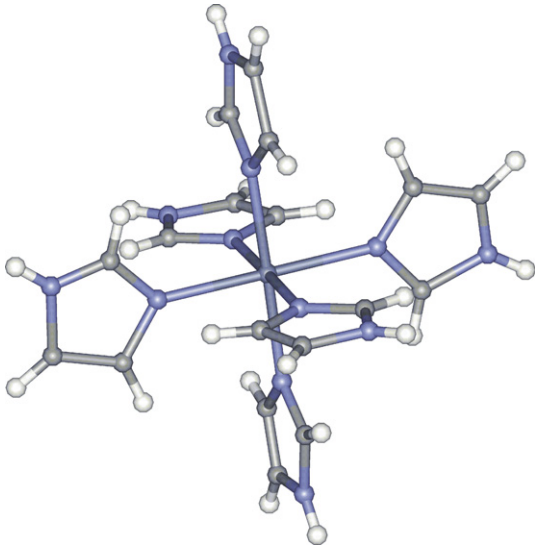

Fig. 1. Structure of the $Mn(Im)_6$ complex. The data have been obtained by X-ray diffractometry and processed with WebLab ViewerPro.

this frequency the magnetic field is high enough for the Zeeman term to dominate the spin Hamiltonian of the system. Consequently, the analysis of the fine structure can be carried out with the ZFS treated as a first-order perturbation.

An FID-detected single crystal EPR spectrum recorded at 10 K is shown in Fig. 2. In this spectrum 54 lines instead of the expected 30 lines are observed. All but the central lines (m_S: $-1/2 \rightarrow 1/2$) are split into doublets with equal intensity. This is caused by the twinning of the crystal with an approximately equal amount of two different centers (center a and b). This effect has already been observed in an earlier study [30] and was attributed to the doping of the crystal with manganese. All split lines correspond to outer transitions involving higher electron spin manifolds. Since the spectrum was taken at low temperature ($T = 10$ K) the population difference between the spin manifolds is readily visible. From the difference in the intensities the sign of the axial ZFS parameter (D) can be deduced, since it represents the main contribution to the fine structure. D was found to be negative, this can be realized even from this particular spectrum, which was taken with a crystal orientation where B_0 is close to z_D, in view of the fact that the $|-5/2\rangle \rightarrow |-3/2\rangle$ transitions are shifted toward lower fields.

To determine the fine structure, the mid-point for each set of hyperfine lines was taken and plotted as a function of the position of the crystal with respect to the external magnetic field. Rotations of 180° were performed in three different planes almost perpendicular to each other (see insets in Fig. 3). The first rotation was performed around the axis perpendicular to the largest face of the crystal (Rot. 1). The second rotation axis was perpendicular to the z-axis of the D tensor (Rot. 2), and the last rotation was carried out around the z-axis (Rot. 3). The

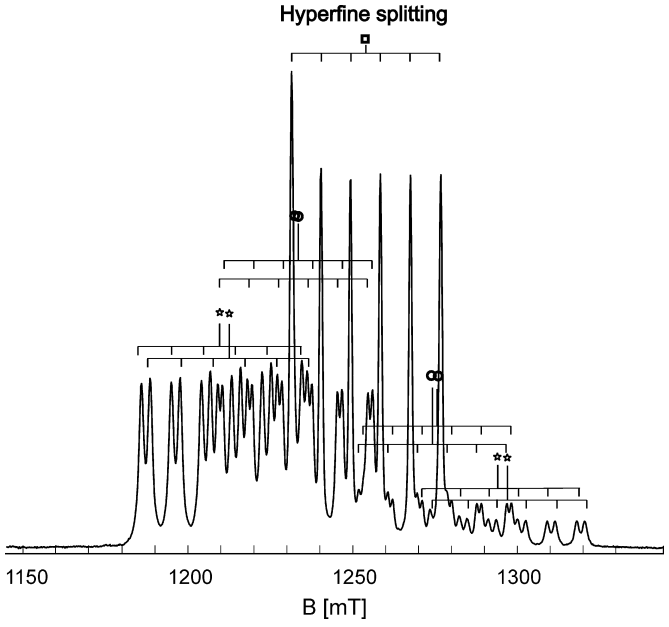

Fig. 2. FID-detected Q-band EPR spectrum for an orientation of the magnetic field close to z_D. The lines corresponding to the same fine-structure level have been grouped. Note the twinning of the crystal, which is revealed by a doubling of the outer lines involving higher electron spin manifolds. Stars: $|\pm\frac{5}{2}\rangle \leftrightarrow |\pm\frac{3}{2}\rangle$ transitions, circles: $|\pm\frac{3}{2}\rangle \leftrightarrow |\pm\frac{1}{2}\rangle$ transitions, squares: $|-\frac{1}{2}\rangle \rightarrow |+\frac{1}{2}\rangle$ transitions.

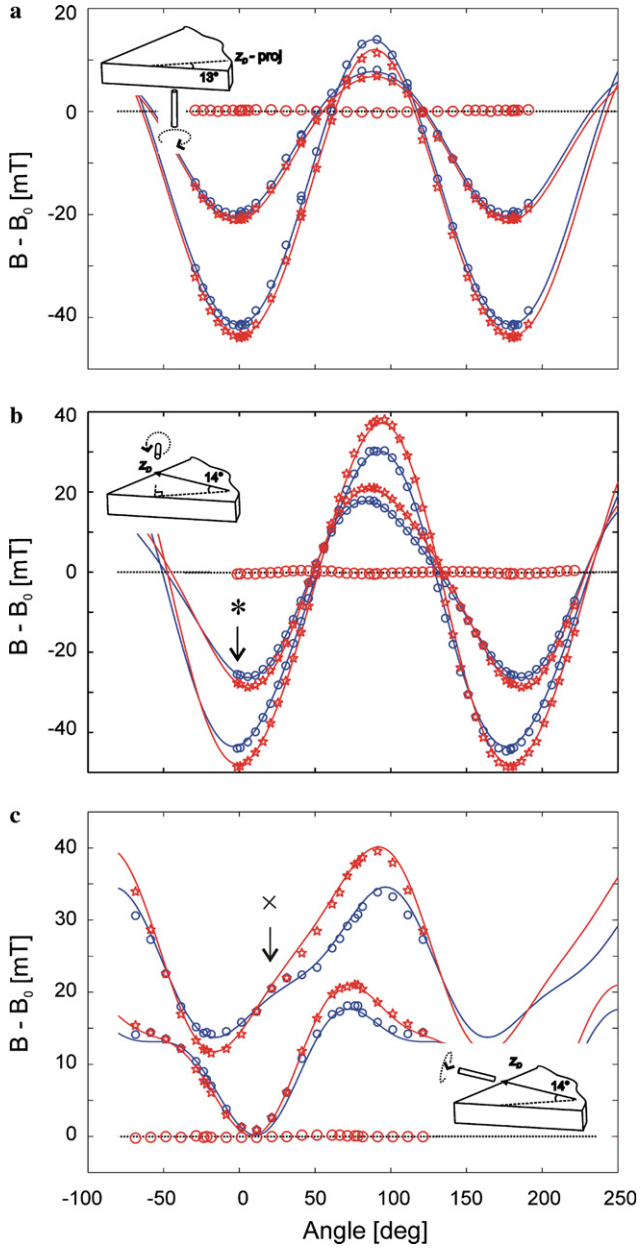

Fig. 3. Rotation diagrams of the $Mn(Im)_6$ complex. The difference between the position of the lines (B) and the magnetic field corresponding to $g = 2$ (B_0) has been plotted as a function of the orientation. The circles represent the position of the experimental lines of center a and the stars the ones of center b, the central lines (which barely change position with the rotation angles) are represented by circles but they correspond to both centers. The solid lines are the calculated rotation patterns obtained using the parameters given in Table 1. (a) Rotation pattern 1 (Rot. 1); (b) Rotation pattern 2 (Rot. 2); (c) Rotation pattern 3 (Rot. 3). The insets indicate the rotation axes for each of the diagrams. The orientation labeled with an asterisk is the one at which the spectra of Fig. 5 were taken. The orientation labelled with a cross is the one corresponding to the spectrum in Figs. 6 and 7.

rotation diagrams are displayed in Fig. 3. The positions of the lines representing the m_S: $1/2 \rightarrow 3/2$ and m_S: $3/2 \rightarrow 5/2$ transitions have been omitted as they are symmetric to the transitions m_S: $-3/2 \rightarrow -1/2$ and m_S: $-5/2 \rightarrow -3/2$, respectively.

The first rotation diagram (Fig. 3a) was performed by rotating the magnetic field within the large face of the crystal. Assuming that the most important contribution to the splitting between the different electron spin manifolds originates from the third term in Eq. (2), the orientation with the maximum splitting corresponds to the projection of the z-axis of the D tensor (z_D) onto this plane. For the first rotation diagram this happens at 13° from the x_R habitus axis of the crystal. In the second rotation pattern the magnetic field was rotated in a plane perpendicular to the first rotation plane containing the previously determined projection of z_D on the face of the crystal. The direction of maximum splitting in this pattern determines z_D, which forms angles of 14° and 16.5° with respect to the crystal plane for centers a and b, respectively. Once the direction of z_D was determined in this way, the third rotation pattern was measured using z_D as the rotation axis of the crystal perpendicular to the external magnetic field.

As already implicitly mentioned in the theoretical section, the spin Hamiltonian of the system has ten independent parameters to adjust; namely, the ZFS parameters D and E, three angles to locate the axes of the D tensor with respect to the laboratory axes, the parameters a and F, and the three angles that position the cubic axes with respect to any other coordinate system. To reduce the number of parameters that have to be adjusted simultaneously, it is worth noting that the quantity

$$F = \tfrac{5}{4}B\left(\left|\pm\tfrac{5}{2}\right\rangle \leftrightarrow \left|\pm\tfrac{3}{2}\right\rangle\right) + B\left(\left|\pm\tfrac{3}{2}\right\rangle \leftrightarrow \left|\pm\tfrac{1}{2}\right\rangle\right) - \tfrac{9}{2}B_0 = \tfrac{7}{2}\left[D\left(3\cos^2\theta - 1\right) + 3E\sin^2\theta\cos 2\phi\right] \quad (6)$$

only depends on the second-rank ZFS, whereas the quantity

$$G = B\left(\left|\pm\tfrac{5}{2}\right\rangle \leftrightarrow \left|\pm\tfrac{3}{2}\right\rangle\right) - 2B\left(\left|\pm\tfrac{3}{2}\right\rangle \leftrightarrow \left|\pm\tfrac{1}{2}\right\rangle\right) + B_0 = \tfrac{7}{12}Fq + 7a\Omega \quad (7)$$

only contains parameters of the forth-rank term of the ZFS. This allowed us to divide the fitting procedure into two independent steps, varying only four or five independent parameters at the same time. The experimental values of the quantities F and G and their corresponding best fits are shown in Fig. 4. The resulting values of the parameters for both centers are given in Table 1. Note that the two centers differ from each other in their values D and E, while the orientation of the two D tensors is only slightly different. On the other hand, the G quantities for the two centers could be predicted with the same parameters, since the experimental values of G for both centers are the same at all orientations within error limits. The dominating octahedral symmetry of the complex suggests that the axes of the cubic contribution

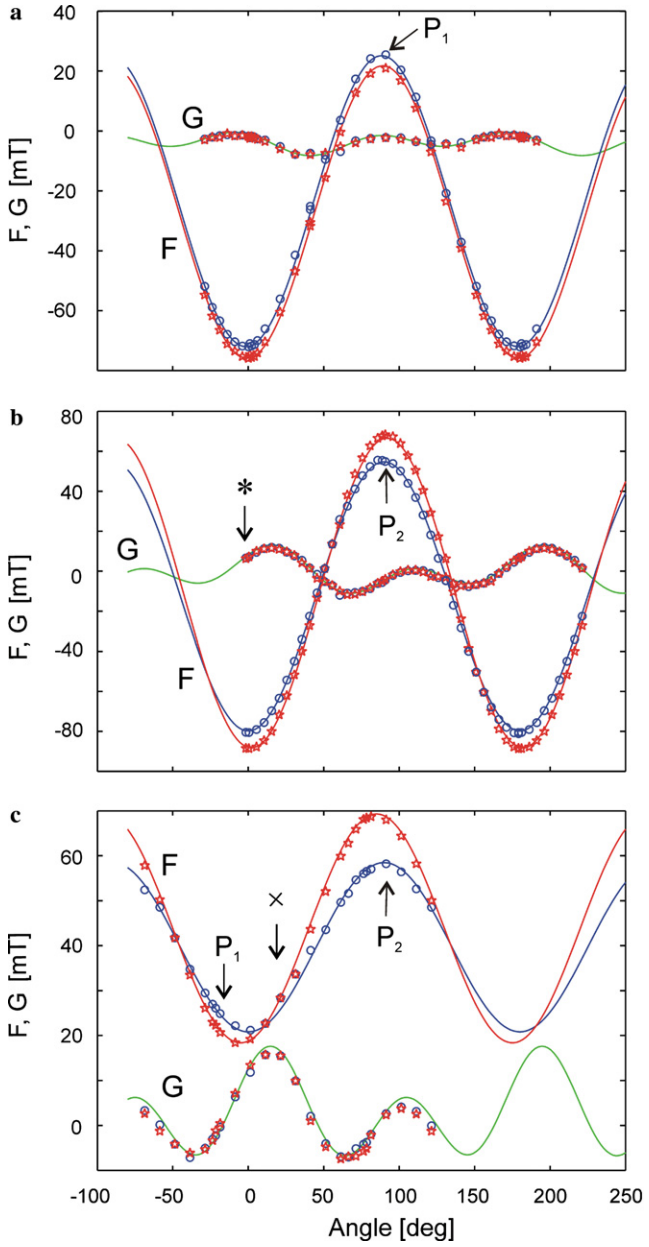

Fig. 4. Rotation pattern of the derived quantities F and G (for definition see text) in the three rotation planes used in Fig. 3. Open circles and stars represent the experimental values for center a and b, respectively. The solid lines are fittings to the experimental values with the parameters given in Table 1. (a) Rotation pattern 1 (Rot. 1); (b) Rotation pattern 2 (Rot. 2); (c) Rotation pattern 3 (Rot. 3). The asterisk and the cross label the orientations at which spectra in Figs. 5 and 6 were taken, respectively. The orientations at which the magnetic field is perpendicular to z_D in Rot. 1 and Rot. 2 are labeled P_1 and P_2, respectively.

of the ligand field (cubic axes) correspond to the molecular symmetry axes, namely, the directions between the manganese ion and its imidazole ligands. This indicates that in both twins the molecular axes are the same, so that both complexes have the same orientation. Consequently, it seems that the twinning of the crystals causes just slightly different D tensors in the two twin structures.

Table 1
Spin Hamiltonian parameters for the two centers in the crystal

	D	E	α_D	β_D	γ_D	F	a	α_C	β_C	γ_C
Center a	-106 ± 2	-17 ± 1	13 ± 2	76 ± 3	108.5 ± 5	5 ± 3	24 ± 2	180 ± 4	55 ± 4	-141 ± 11
Center b	-118 ± 2	-22 ± 1	14 ± 2	73.5 ± 3	103.5 ± 5					

The values of D, E, F and a are given in 10^{-4} cm^{-1}. The Euler angles of the D tensor (labeled with the subscript D) and those of the cubic axes (subscript C), both with respect to the axes of the crystal, are given in degrees.

3.2. HYSCORE

The hyperfine interactions of the electron spins of Mn(II) with the nuclear spins of the surrounding nitrogens were studied by means of HYSCORE spectroscopy performed at Q-band [4]. In this 2D experiment pairs of peaks are observed symmetrically placed with respect to the main diagonal. Each dimension corresponds to a nuclear frequency in an electron spin manifold that is connected by the EPR transition to another electron spin manifold, with $\Delta m_S = 1$.

Typically, the HYSCORE spectra were measured at three different field positions, containing the transitions $|-\frac{5}{2}\rangle \rightarrow |-\frac{3}{2}\rangle$, $|-\frac{3}{2}\rangle \rightarrow |-\frac{1}{2}\rangle$, or $|-\frac{1}{2}\rangle \rightarrow |\frac{1}{2}\rangle$. Fig. 5 depicts the spectra measured for B_0 parallel to z_D. This orientation is labeled with an asterisk in Fig. 3. The spectrum in Fig. 5a

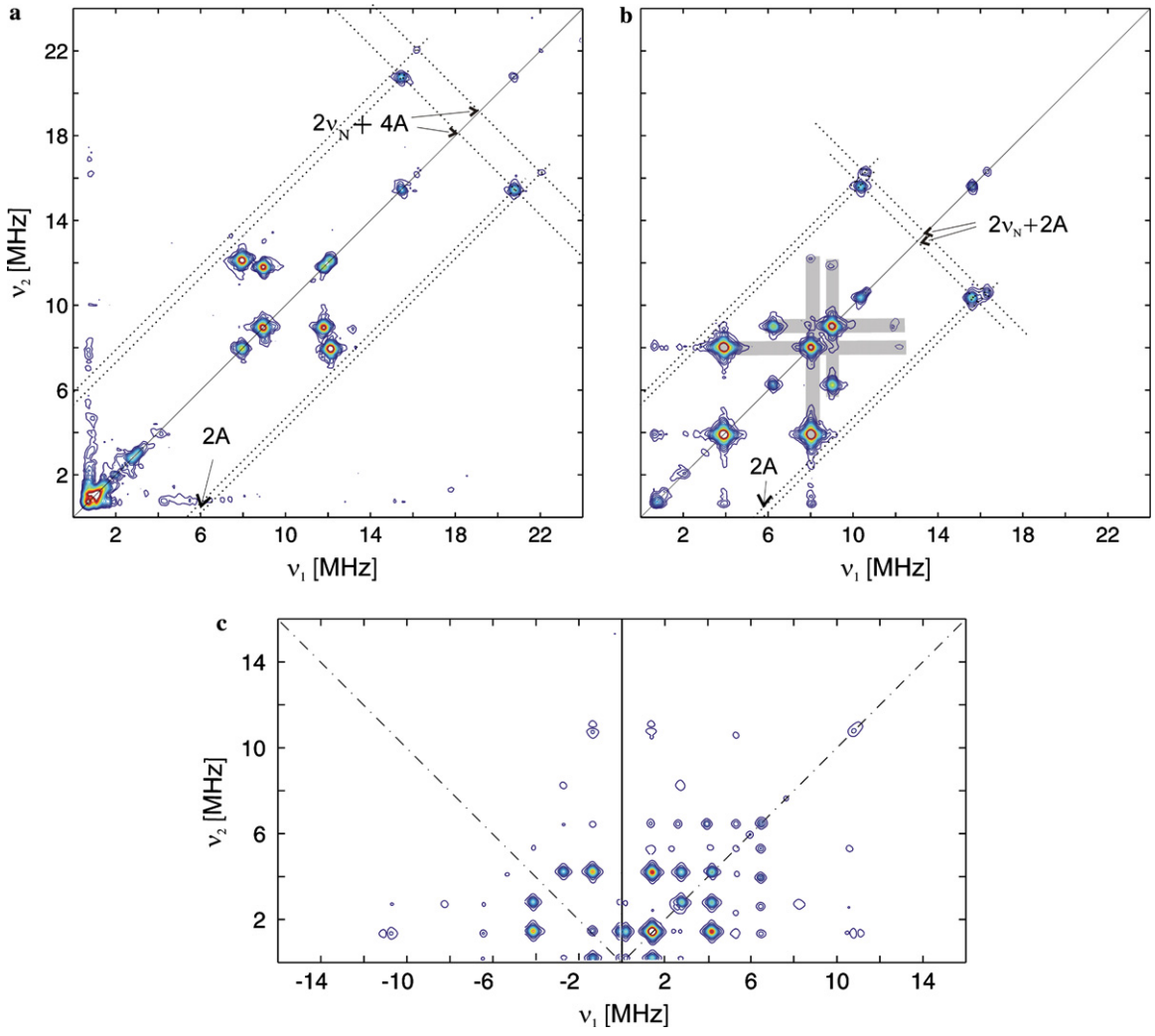

Fig. 5. Q-band HYSCORE spectra of Mn(Im)$_6$ recorded at one of the electron spin transitions: (a) $m_S : |-\frac{5}{2}\rangle \rightarrow |-\frac{3}{2}\rangle$, $B_0 = 1183$ mT, $\tau = 208$ ns; (b) $m_S : |-\frac{3}{2}\rangle \rightarrow |-\frac{1}{2}\rangle$, $B_0 = 1179$ mT, $\tau = 208$ ns; (c) $m_S : |-\frac{1}{2}\rangle \rightarrow |+\frac{1}{2}\rangle$, $B_0 = 1251$ mT, $\tau = 96$ ns. The magnetic field for all spectra is parallel to the z-axis of the D tensor (z_D). This orientation is labeled with an asterisk in the rotation patterns shown in Figs. 3, 4 and 8. The nuclear frequencies in correlation patterns a and b can be calculated in a first-order approximation. In this case the hyperfine coupling constant can be directly extracted from the spectrum tracing a line parallel to the diagonal from the dq peaks. The value where this line crosses the abscissa is 2A. If a line perpendicular to the diagonal is drawn, it crosses the diagonal at $2\nu_N + 4A$ for the $|-\frac{5}{2}\rangle \rightarrow |-\frac{3}{2}\rangle$ transitions and at $2\nu_N + 2A$ for $|-\frac{3}{2}\rangle \rightarrow |-\frac{1}{2}\rangle$. In spectrum b the crosses formed by the sq peaks (see text) have been highlighted.

corresponds to the outermost of the transitions $|-\frac{5}{2}\rangle \rightarrow |-\frac{3}{2}\rangle$. Several cross-peaks can be observed in the (+,+) quadrant. Those with the frequencies (20.8, 15.5) MHz and (22.0, 16.2) MHz seem to fulfill the first expression in Eq. (5), since five times the higher frequency minus three times the lower frequency is approximately four times the nuclear Larmor frequency of ^{14}N, $\nu_N = 3.64$ MHz for this field position. These cross-peaks are consequently assigned to the double-quantum (dq) frequencies of two ^{14}N nuclei with slightly different hyperfine interactions. The cross-peaks at lower frequencies are assigned to single-quantum (sq) transitions in both manifolds. After performing a complete analysis of the data (see below) the peaks can be assigned to three different nuclei.

The spectrum in Fig. 5b was recorded at one of the transitions $|-\frac{3}{2}\rangle \rightarrow |-\frac{1}{2}\rangle$; again the correlations observed at higher frequencies are assigned to dq–dq frequencies and the other peaks to sq-sq frequencies. Note that the two most intense pair of peaks in the spectrum in Fig. 5a at (11.8, 9.0) MHz and (12.1, 7.9) MHz are also (weakly) visible in the spectrum in Fig. 5b. This is because the excitation is not completely selective to the chosen $|-\frac{3}{2}\rangle \rightarrow |-\frac{1}{2}\rangle$ transition and the microwave pulses also excite one of the $|-\frac{5}{2}\rangle \rightarrow |-\frac{3}{2}\rangle$ transitions of centre *b*, whose resonance field is close to the one set for the experiment. This pair of peaks is located in the spectrum in a way that, together with the sq-sq cross-peaks at (9.0, 6.3) and (7.9, 4.0) MHz, they form crosses with the two peaks sharing one of its frequencies. Indeed, frequencies belonging to the $m_S = -3/2$ manifold can be observed in the spectra in Fig. 5a and Fig. 5b, since both transitions have a level of this manifold in common. Most of the peaks in the spectrum in Fig. 5a have one of the frequencies in common with a peak in the spectrum in Fig. 5b (except for a small difference which is attributed to the shift of the magnetic field). In this way some of the nuclear frequencies can be tracked down in the different electron spin transitions. On the other hand, the fact that the crosses above mentioned have a very regular shape (the four endpoints are all equidistant from the intersection of the cross), means that the frequency differences in the $m_S = -3/2$ and the $m_S = -5/2$ manifold are the same as the frequency differences in the $m_S = -3/2$ and the $m_S = -1/2$ manifold, which is consistent with the first-order approximation (see Eq. (5)).

The lines in the spectrum corresponding to the transition $|-\frac{1}{2}\rangle \rightarrow |\frac{1}{2}\rangle$ (Fig. 5c) are more intense and can be observed in both quadrants. The spectrum is dominated by sq-sq cross-peaks at (4.15, 1.35) MHz tracked down from the most intense peak in the spectrum in Fig. 5b, another sq–sq peak appears at (6.45, 3.95) MHz. In addition a set of dq–dq peaks is observed at (10.8, 5.30) MHz, but their intensity is very low and the peaks are not further resolved. In this spectrum also a large number of combination peaks are observed, whose frequencies are sums or differences of basic nuclear frequencies in the same electron spin manifold (see Table 2). For example, a correlation peak can be found at (8.3, 2.7) MHz, with frequencies twice as large as the ones of the most intense sq–sq peaks. The presence of such peaks at the double frequencies implies the existence of (at least) two equivalent nuclei.

Table 2
Frequencies and assignation of the correlation peaks appearing in spectrum 5c

	Peak frequencies	Nucleus	Correlation type
Basic frequencies	(4.15, 1.35)	N1	sq–sq
	(6.45, 3.95)	N3	sq–sq
	(10.80, 5.30)	N3	dq–dq
Combination frequencies	(4.15, 2.70)	N1	sq–2dq
	(6.45, 1.35)	N3, N1	sq–sq
	(6.45, 2.70)	N3, N1	sq–2dq
	(6.45, 5.35)	N3, N1	sq–sq+sq
	(8.30, 2.70)	N1	2dq–2dq
	(10.80, 1.35)	N3, N1	dq–sq
	(11.10, 1.35)	N2, N1	dq–sq

The spectra at other field orientations look similar, reduction of resolution and strengthening of the combination peaks being a common behavior when going from outer to central transitions. No difference was observed between HYSCORE spectra of centers a and b. The echoes of the transitions $|+\frac{1}{2}\rangle \rightarrow |+\frac{3}{2}\rangle$ and $|+\frac{3}{2}\rangle \rightarrow |+\frac{5}{2}\rangle$ are weaker, since the corresponding levels are sparsely populated under the experimental conditions. It was therefore difficult to follow these transitions as a function of the orientation and systematically measure the HYSCORE spectra. Nevertheless, a HYSCORE spectrum of the $|+\frac{1}{2}\rangle \rightarrow |+\frac{3}{2}\rangle$ transition could be measured (Fig. 6) for the orientation labeled by a cross in Fig. 3.

The most striking feature of this 2D spectrum is the abundance of intense cross-peaks in both quadrants. For the most intense peaks one of the frequencies is below 2.7 MHz; which represents nuclear transitions in the $m_S = +3/2$ manifold. The frequencies of the $m_S = +1/2$ manifold can be traced from the $|-\frac{1}{2}\rangle \rightarrow |+\frac{1}{2}\rangle$ spectrum, and peaks with twice or even three times these frequencies become visible, generating the regular pattern in the spectrum. The spectrum is consistent with two pairs of different nitrogen nuclei, which are very close to the exact cancellation condition in the $m_S = +3/2$ manifold ($A \approx 3/2\nu_N$). Both sets of nuclei (N1 and N2 as assigned in Table 3) happen to have approximately the same nuclear frequencies in the $m_S = +1/2$ manifold.

Fig. 7 shows the first time trace of the HYSCORE spectra for the same orientation as in Fig. 6 and the transitions $|-\frac{5}{2}\rangle \rightarrow |-\frac{3}{2}\rangle$, $|-\frac{3}{2}\rangle \rightarrow |-\frac{1}{2}\rangle$, $|-\frac{1}{2}\rangle \rightarrow |+\frac{1}{2}\rangle$, and $|+\frac{1}{2}\rangle \rightarrow |+\frac{3}{2}\rangle$. The modulation is very shallow for the $|-\frac{5}{2}\rangle \rightarrow |-\frac{3}{2}\rangle$ transitions, increases for the $|-\frac{3}{2}\rangle \rightarrow |-\frac{1}{2}\rangle$ transitions and is very deep in the other two.

To characterize the hyperfine interactions, HYSCORE spectra were measured for different orientations within the previous rotation patterns. Several spectra were taken with the magnetic field perpendicular to z_D (Rot. 3). In this plane, the projection of the magnetic field onto the plane $x_C z_C$ of the cubic reference frame forms an angle of approximately 30° with the axis x_C. In Rot. 3 the

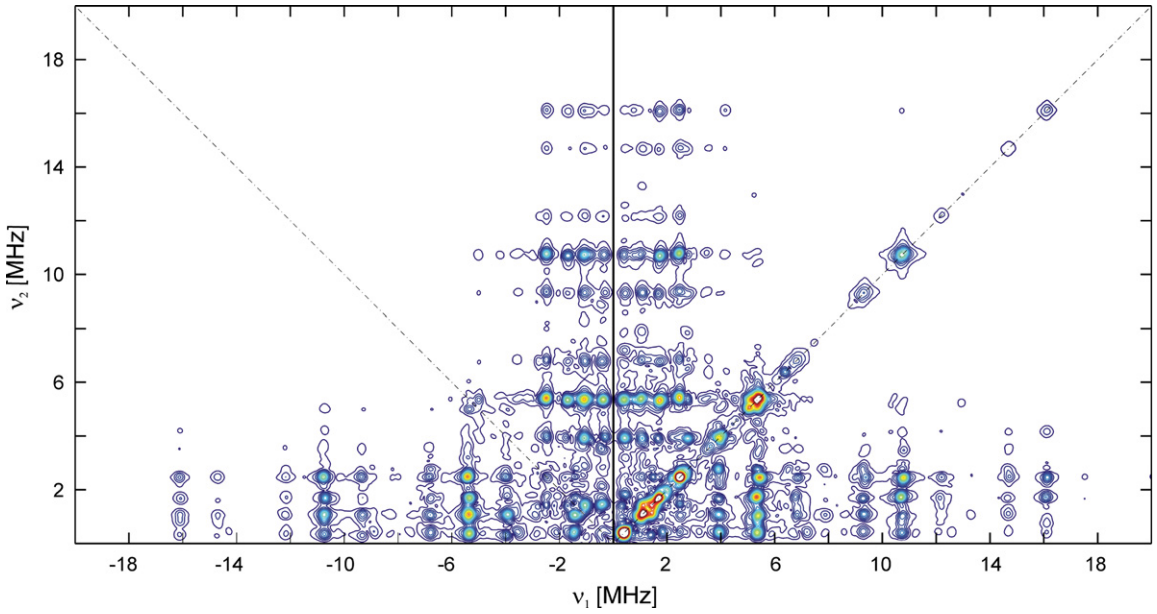

Fig. 6. Q-band HYSCORE spectrum of $Mn(Im)_6$ for one of the electron spin transitions $m_S : |+\frac{1}{2}\rangle \rightarrow |+\frac{3}{2}\rangle$, $\tau = 208$ ns. The magnetic field is close to the cubic axis y_C, which correspond to an angle of 22° in Rot. 3. This orientation is labeled with a cross in the rotation patterns of Figs. 3, 4 and 8.

Table 3
Principal values of the hyperfine and nuclear quadrupole tensors of the three pairs of ^{14}N atoms coordinating Mn(II) in $Mn(Im)_6$

	N1	N2	N3
Q_X	0.7	−1.5	0.8
Q_Y	0.8	0.5	−1.5
Q_Z	−1.5	1.0	0.7
A_X	2.50	4.37	2.75
A_Y	2.62	2.65	4.40
A_Z	4.45	2.64	2.60
A_{iso}	3.19	3.22	3.25
$2T$	1.26	1.15	1.15
$2T_{cal}$	($r = 2.19$ Å)		1.09
$2T_{cal}$	($r = 2.27$ Å)		0.98

The principal directions are assumed to be the Mn–N binding directions. The values are given in MHz and the errors in the parameters have been estimated to be ±0.1 MHz. $2T$ denotes the anisotropic hyperfine contribution in the binding direction and $2T_{cal}$ the one calculated in the point-dipole approximation.

magnetic field is approximately along the axis y_C at a rotation angle ≈ 13°. The values of the nuclear frequencies were extracted from the different spectra and assigned by tracing them down and by comparing them with the calculated values (see below). Plots of the nuclear frequencies versus rotation angle are presented in Fig. 8a for dq frequencies and in Fig. 8c for sq frequencies. In addition, HYSCORE measurements were carried out for magnetic field orientations with z_D in the rotation plane (Rot. 2), which contains the direction closest to the cubic axis z_C of all three rotations. The corresponding nuclear frequencies are displayed in Figs. 8b and d. Considering all experimental spectra, six nitrogen

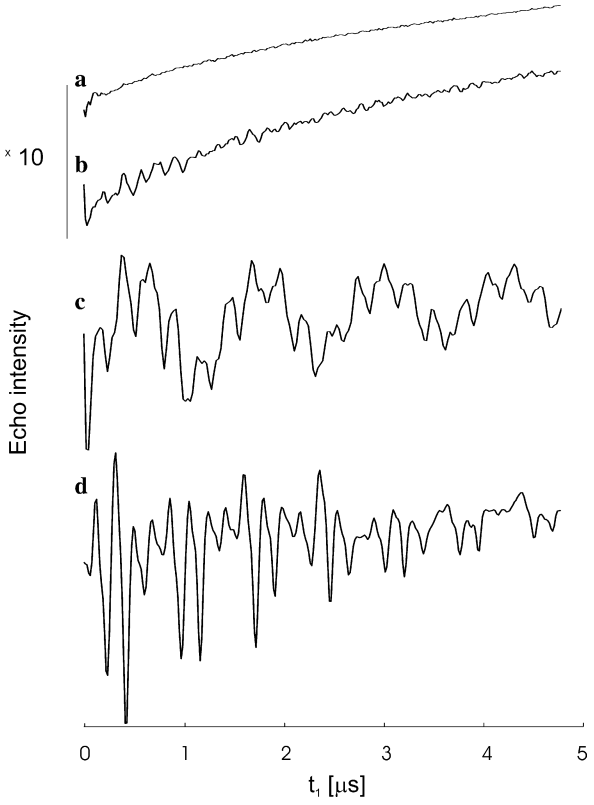

Fig. 7. First trace of Q-band HYSCORE spectra for different electron spin transitions. (a) $m_S : |-\frac{5}{2}\rangle \rightarrow |-\frac{3}{2}\rangle$, $\tau = 144$ ns, (b) $m_S : |-\frac{3}{2}\rangle \rightarrow |-\frac{1}{2}\rangle$, $\tau = 144$ ns. Note that traces (a) and (b) have been multiplied by a factor of 10, (c) $m_S : |-\frac{1}{2}\rangle \rightarrow |+\frac{1}{2}\rangle$, $\tau = 144$ ns, (d) $m_S : |+\frac{1}{2}\rangle \rightarrow |+\frac{3}{2}\rangle$, $\tau = 208$ ns. The orientation of the magnetic field is the same as for the previous spectra in Figs. 6, labeled with a cross in Figs. 3, 4 and 8.

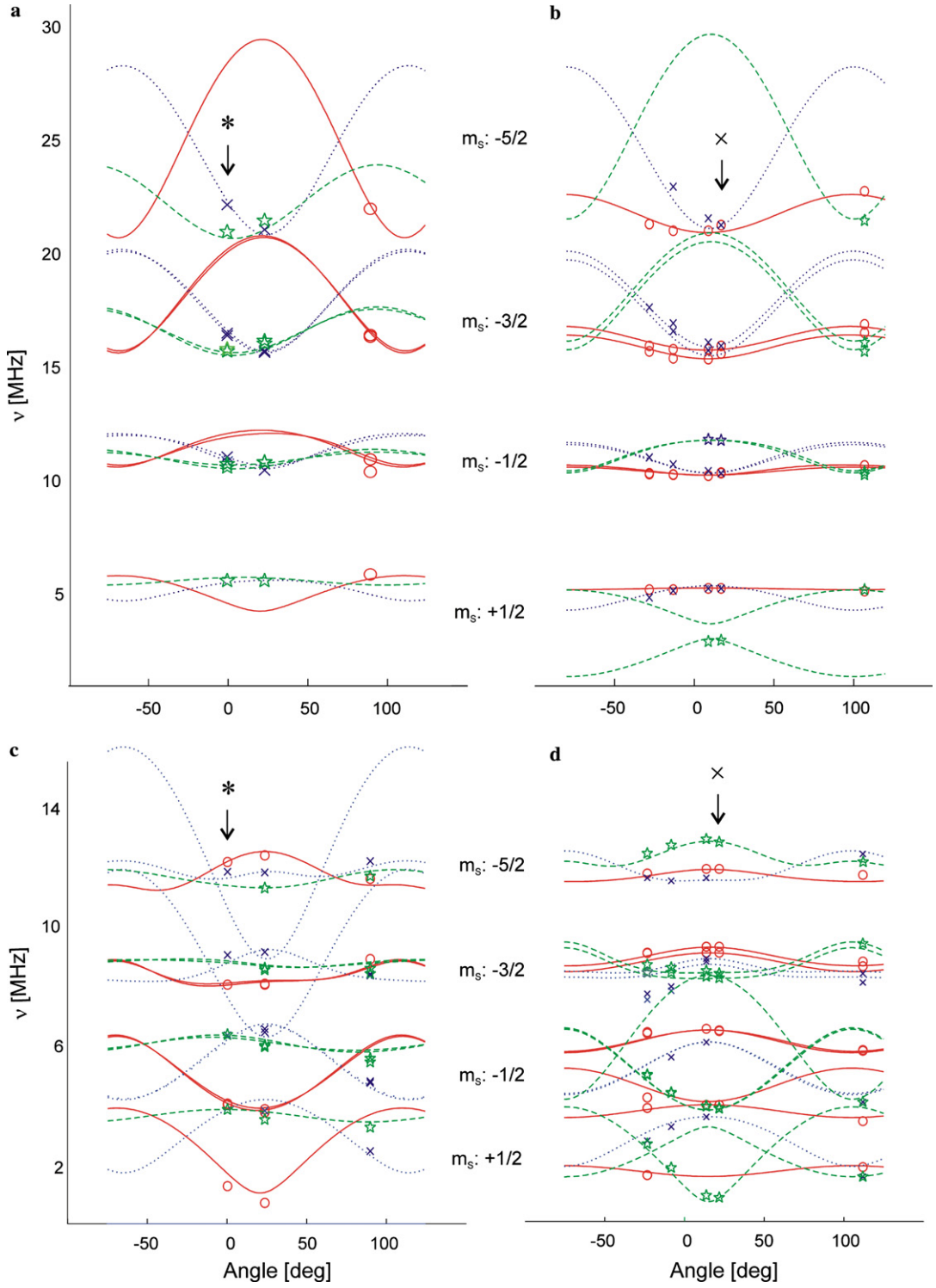

Fig. 8. ^{14}N nuclear frequencies of the probed electron spin manifolds as a function of the orientation. The experimental points are displayed as: open circles when the nuclear frequency is assigned to the pair of nuclei N1, crosses for nuclei N2 and stars for N3. The lines represent the fittings using the parameters shown in Table 3; solid line for N1, dotted line for N2, and dashed line for N3. (a) Rotation 3: dq frequencies, (b) Rotation 2: dq frequencies, (c) Rotation 3: sq frequencies, and (d) Rotation 2: sq frequencies. All the sq frequencies were calculated but only the ones needed to fit the experimental points have been displayed. The electron spin manifold to which the nuclear frequencies belong is also indicated. Some of the experimental points and calculated lines are doubled due to the fact that certain nuclear frequencies are detected for two different electron spin transitions.

nuclei equivalent in pairs are found. Each pair of equivalent nitrogen nuclei had to be identified as the diametrically opposed pairs of coordinating nitrogens.

The hyperfine and nuclear quadrupole couplings for the three pairs of magnetically equivalent nitrogens are given in Table 3. Several assumptions were made to find these

parameters. First, since the cubic axes coincide with the axes of the octahedral crystal field, it is expected that they correspond to N–Mn binding directions. Second, it seems reasonable that the bonding axes of such a symmetrical structure are also principal axes of the hyperfine and nuclear quadrupole tensors of the coordinated nitrogen nuclei. As a first working hypothesis we considered all six nitrogen nuclei as geometrically equivalent, the nuclear spin Hamiltonian parameters were preliminary calculated with Eq. (5) and then refined by fitting the patterns in Fig. 8 to the nuclear spin Hamiltonian in Eq. (4).

4. Discussion

By fitting the rotation patterns of the FID-detected or echo-detected EPR spectra, we have shown in the previous section how the orientation of the D tensor axes and the cubic axes could be determined with respect to the crystal-fixed reference frame. However, the optimum fitting requires for every rotation pattern a slightly different orientation of the two sets of axes mentioned above; this is due to small misorientations of the crystal, giving rise to small errors in the determination of the Euler angles.

To get an estimate of the misorientation, we considered the rotation pattern Rot. 3, which contains the orientations of the magnetic field that are perpendicular to z_D. The rotation patterns Rot. 1 and Rot. 2 also contain one direction in which the magnetic field is perpendicular to z_D; for Rot. 1 this direction (labeled P_1 in Fig. 4) is at 90° of the projection of z_D in the plane of the crystal. In Rot. 2 this orientation has been labeled as P_2 in Fig. 4. As P_1 is the axis of rotation of Rot. 2, both directions are perpendicular to each other and both of them should be reproduced in Rot. 3. Indeed, the spectra taken at −18.5° and 76.5° (labeled as P_1 and P_2 in Fig. 4c) approximately replicate those of Rot. 1 and Rot. 2; however, their orientations differ by 95° rather than by 90° as expected for a perfectly positioned crystal. Therefore, we have allowed for a ±5° error in the angles describing the position of the crystal. The errors given in Table 1 have been determined so that when the angles of the sample holders are varied ±5° and the rotational patterns are fitted again, the new set of parameters stays within the error margin.

For this study rhombic crystals were chosen. As the shape of the unit cell replicates the shape of the crystal, the edges of the flat crystal correspond to the directions of the unit cell sides a and b. Furthermore, the orientation of the cubic axes with respect to the crystal macroscopic axes found here (Table 1) coincide with the orientation of the molecular axes with respect to the unit cell known from the X-ray studies of the complex [27,28]. This confirms the identity of the cubic and molecular axes.

The origin of the D tensor is not completely clear yet. Note however, that the axes of the D tensor do not coincide with the axes of the molecule and the two sites have slightly different D tensors, but the same orientation of the molecular axes and the same HYSCORE spectra. It therefore seems that the second-rank ZFS is caused by the electrostatic interactions of the metal with the counter ions. From the crystal structure it can be seen that for every Mn^{2+} ion the surrounding Cl^- ions can be arranged in pairs at the same distance and diametrically opposed with respect to the metal. The closest pair is found at about 6 Å but the direction along which they are aligned does not coincide with any of the D tensor principal axes. Four additional pairs of Cl^- ions are positioned between 7.20 and 7.90 Å and oriented along different directions. However, their possible contribution to the ZFS is not evident without a detailed study of the crystal field, which is beyond the scope of this paper.

Note that in a previous cw-EPR study of this complex [30] the parameters reported differ considerably from the ones presented in this work. The authors fit their experimental data with an axial D tensor collinear to the cubic axes. Since the studies have been carried out in different temperature ranges, a potential phase-transition might be responsible for this discrepancy. However, the authors in [30] were unable to follow the transitions $|\pm\frac{3}{2}\rangle \rightarrow |\pm\frac{1}{2}\rangle$, which is crucial to find the relative orientations between the cubic axes of distortion and the principal axes of the D tensor.

Compared to other Mn(II) complexes the value of $|D|$ is small. This is not surprising as the molecular symmetry is nearly octahedral and the anions that are probably responsible for the non-cubic ZFS are relatively remote. On the other hand, the value found for the parameter a is larger than the one observed in other complexes where Mn(II) is coordinated by oxygen atoms. In these cases the cubic contribution to the ZFS was not needed to explain the spectra [31–33]. The most likely reason for the larger a value found in our work is that nitrogen ligands are stronger electron donors. Consequently, the crystal field of octahedral symmetry probed by the metal is stronger as well. This happened to be quite helpful because the cubic contribution to the ZFS allows us to locate the molecular axes, which was useful for the study of the nitrogen hyperfine interactions.

To examine the hyperfine couplings for a certain magnetic field orientation, it seems to be redundant to measure HYSCORE spectra of several transitions, since in principle, they contain the same information. Nevertheless, this procedure turned out to be effective given that tracking the nuclear frequencies facilitated their assignment. Moreover, the peak intensities are different for different electron spin transitions due to the different relative weight of the hyperfine term in the Hamiltonian. Consequently, measuring HYSCORE on several transitions allows the detection of a larger number of nuclear frequencies. This is similar to the effect of carrying out experiments at several microwave frequencies. Thus, in the spectra corresponding to the $|-5/2\rangle \rightarrow |-3/2\rangle$ and $|-3/2\rangle \rightarrow |-1/2\rangle$ transitions, there are correlations from all three sets of nuclei, although the spectra corresponding to the $|-1/2\rangle \rightarrow |+1/2\rangle$ transitions are normally dominated by lines of a single set of nuclei. In

addition, quite strong combination lines appear in this spectrum. In HYSCORE experiments on the transitions $|+1/2\rangle \rightarrow |+3/2\rangle$, the spectra are so rich in cross-peaks, that data from other transitions are required for an unequivocal interpretation.

For the first two electron spin transitions the hyperfine and nuclear Zeeman interactions dominate the nuclear Hamiltonian and consequently the first-order approximation given in Eq. (5) is applicable, especially when the direction of the magnetic field is along one of the molecular axes. Then, the simple graphical recipe shown in Fig. 5a and b can be helpful. Note that despite the large value of $|A_{\text{eff}}| = 5\text{A}$ or $3\text{A} > 2\nu_{\text{N}}$, all the peaks appear in the $(+,+)$ quadrant, because for each electron spin manifold the directions of the effective magnetic field at the nucleus are close to each other. In contrast, for the other electron spin transitions, the off-diagonal contributions to the nuclear Hamiltonian of the nuclear quadrupole interaction are not negligible and consequently the first-order expressions for the nuclear frequencies are no longer valid.

The peak intensities in the HYSCORE spectra are affected by the value of the hyperfine interaction as well. This is shown in Fig. 7, where the modulation depth diminishes as one moves away from the exact cancellation condition.

The values of the ^{14}N parameters in Table 3 have been obtained from the best fitting of the data presented in Fig. 8. The error intervals displayed there mean that the fitting is still acceptable for values of the parameters within this range. Nevertheless, they should not be taken as a measure of the precision of the parameters, because other factors like misorientation of the crystal and the presence of off-diagonal elements in the coupling tensors also influence the accuracy of the fitting, and may cause small unknown systematic errors in the stated values. However, since the fitting results are acceptable our initial assumptions appear to be correct, i.e., the principal axes of the hyperfine and nuclear quadrupole tensors approximately coincide with the molecular axes.

The hyperfine principal values, which are very similar for all three pairs of nitrogens, can be decomposed into an isotropic, $A_{\text{iso}} \approx 3.2$ MHz, and a nearly axially symmetric anisotropic contribution. The positive sign of the hyperfine couplings has been experimentally determined and reveals a positive spin density in the nucleus of the ligands. Two of the metal semioccupied orbitals have a σ^* character and are classified as e_{g} according to their symmetry [34]. These orbitals have some admixture of the nitrogen 2s orbitals which is most probably responsible for the observed positive spin density. Table 3 also includes data obtained from the point-dipole approximation for average distances Mn–N between 2.20 Å (Zn–N distance from the crystal structure of $Zn(Im)_6$ [27]) and 2.27 Å (Mn–N distance in the pure $Mn(Im)_6$ crystal [28]). In general the point-dipole approximation is valid when the distance between the electron and the nuclear dipole is larger than 2.50 Å.

It would be surprising if in a molecule of such a high symmetry the principal values of the nuclear quadrupole interaction of the different nitrogens differed from each other. So, we have to consider that the observed differences in the quadrupole tensor between the three pairs of nitrogens might not be significant. The nuclear quadrupole tensor of the imino nitrogen of imidazole in the crystal $[Zn(Im)_6]Cl_2{\cdot}4H_2O$ has been measured by nuclear quadrupole resonance (NQR) [35]. The authors found the principal values and principal directions: −1.4 MHz along the Zn–N direction, 0.52 MHz perpendicular to the imidazole plane, and 0.88 MHz in the imidazole plane perpendicular to the binding direction with the metal. These values are within our error limits, confirming the suggestion of the authors that for six imidazoles coordinated to the metal, the population of the donor orbital, and thus, the nuclear quadrupole coupling constants are independent of the metal. The corresponding values for the nitrogen of a histidine residue bound to Fe(III), isoelectronic to Mn(II), found in a single-crystal study of myoglobin [36] are −1.12, 0.31 and 0.81 MHz along the directions described above. These values do not correspond exactly with those found here but it seems obvious that the porphyrin ring coordinating the iron more tightly will cause different electric field gradients.

5. Conclusions

Information about the Mn–Im bonding was obtained by means of the complete characterization of the hyperfine and nuclear quadrupole tensors of the six directly coordinated nitrogens of the model complex $Mn(Im)_6$. This was accomplished using single crystals of the complex and *Q*-band HYSCORE spectroscopy. The hyperfine interaction was decomposed in an isotropic contribution that accounts for the spin density in the ^{14}N nuclei and an almost axial anisotropic contribution that is roughly described by the point dipolar approximation. The nuclear quadrupole tensor was found to be close to the ones reported earlier for single crystals of $Zn(Im)_6$ using NQR. The analysis of the ZFS of the crystal revealed the importance of electrostatic interactions in determining the *D* tensor. The cubic contribution to the ZFS interaction was used as an internal label for the molecular orientation. The determination of the orientational dependence of the hyperfine interactions reveals the nature of the Mn-Imidazole bond and will be of great help for the information obtained here can be used as a reference when interpreting the spectra of disordered systems, including biological samples.

6. Experimental

6.1. Preparation and manipulation of the single crystals

An aqueous solution of zinc chloride (0.4 M), manganese chloride (2 mM) and imidazole (4 M) was prepared and adjusted to pH 6.9 with concentrated hydrochloric acid. All the chemicals were used as purchased, except

for the very hygroscopic zinc chloride, which was dehydrated at 100 °C for half an hour under vacuum and then stored under nitrogen. After a few days in an open container, crystals of hexaimidazole zinc(II) dichloride tetrahydrate doped with 0.5% of the corresponding manganese compound were formed. The zinc and manganese complexes have a very similar crystal structure [27,28], making it possible to obtain a magnetically dilute single crystal of the $Mn(Im)_6$ complex. The space group of the zinc complex is P_1 with one molecule per unit cell and cell parameters $a = 10.63$ Å, $b = 9.23$ Å, $c = 8.83$ Å, $\alpha = 119.53°$, $\beta = 96.85°$, and $\gamma = 97.87°$. All doped crystals showed an approximate 50:50 ratio of racemic twins, both in the X-ray analysis as well as in their EPR behavior (*vide supra*). This behavior of the guest complex has already been observed before [30]. The structure of the complex is shown in Fig. 1.

Rhombic crystals with a thickness of approx 0.5 mm and a length of about 2.5 mm along each rhombic edge were selected for the experiments. They were fixed in different specially tailored Teflon holders, whose mounting planes and adjoining edges were cut to the appropriate angles. This allowed the positioning of the crystals in the desired orientations with respect to the magnetic field. The habitus axes of the crystal were taken as follows: z_R is perpendicular to the large face, x_R is the in-plane direction that coincides with one of the edges of the crystal, and y_R is the direction perpendicular to the other two axes.

6.2. Spectroscopy

All measurements were carried out on a home-built pulse *Q*-band spectrometer working in the microwave frequency range 34.5–35.5 GHz [37] and equipped with an Oxford helium gas-flow cryostat CF 935. The home-built resonator [38] allows for sample diameters up to 3.8 mm. All measurements were done at a temperature of 10 K, and signal averaging was performed at a repetition rate of 3.3 kHz. Rotation of the sample was achieved by means of a goniometer fixed to the sample holder.

Field-swept EPR spectra were recorded by measuring the electron spin echo or the FID generated after the following sequences of microwave pulses [39]: in the *two-pulse echo-detected EPR* experiments the sequence, $\pi/2$-τ-π-τ–*echo*, was used with pulse lengths $t_{\pi/2} = 16$ ns and $t_\pi = 32$ ns, and a time delay τ of 208 ns. The whole width of the echo was integrated. In the *FID-detected EPR* experiments, a microwave π-pulse of length 1 μs was used to generate an FID which was fully integrated for detection.

HYSCORE experiments [4,39] were performed using the pulse sequence, $\pi/2$-τ-$\pi/2$ -t_1-π-t_2-$\pi/2$-τ–*echo*, with pulse lengths $t_{\pi/2} = 24$ ns and $t_\pi = 16$ ns. For every experiment the power of the pulses was appropriately set by optimizing the intensity of a two-pulse echo. The time intervals t_1 and t_2 were varied from 112 to 4896 ns in steps of 16 ns for the electron spin transitions $|-5/2\rangle \rightarrow |-3/2\rangle$ and $|-3/2\rangle \rightarrow |-1/2\rangle$, and from 112 to 7288 ns in steps of 24 ns for the central transition $|-1/2\rangle \rightarrow |+1/2\rangle$. An eight-step phase cycle was used to eliminate unwanted echoes [39]. Spectra recorded with several τ values (120, 168 and 232 ns) were measured to avoid blind-spot effects.

6.3. Data manipulation and calculations

The HYSCORE time traces were baseline corrected using a second-order polynomial, windowed with a Hamming function and zero-filled to 1024 points. Then a 2D Fourier transform was applied and the absolute-value spectrum was calculated. The EPR line positions were calculated as a function of the magnetic field by using Eq. (3), which represent first-order field values obtained from the spin Hamiltonian given in Eq. (2). The calculations of the nuclear frequencies were performed by exact diagonalization of the nuclear spin Hamiltonian.

Acknowledgments

This work has been financed by the Swiss National Science Foundation. A.A. thanks Arthur Schweiger and the ETH Zürich for his sabbatical stay during which some of this work was carried out, and acknowledges support from the NHMFL IHRP program. The authors thank Barbara Feuer, Igor Gromov, and Frank Breher for their very helpful technical assistance.

References

[1] C.W. Bock, A.K. Katz, G.D. Markham, J.P. Glusker, Manganese as a replacement for magnesium and zinc: Functional comparison of the divalent ions, Journal of the American Chemical Society 121 (1999) 7360–7372.
[2] A. Horovitz, Y. Fridmann, G. Kafri, O. Yifrach, Review: allostery in chaperonins, Journal of Structural Biology 135 (2001) 104–114.
[3] G.H. Reed, G.D. Markham, EPR of Mn(II) Complexes with Enzymes and Other Proteins, Plenum Press, New York, 1984.
[4] P. Höfer, A. Grupp, H. Nebenführ, M. Mehring, Hyperfine sublevel correlation (Hyscore) spectroscopy—a 2D electron-spin-resonance investigation of the squaric acid radical, Chemical Physics Letters 132 (1986) 279–282.
[5] N.P. Benetis, P.C. Dave, D. Goldfarb, Characteristics of ESEEM and HYSCORE spectra of $S > 1/2$ centers in orientationally disordered systems, Journal of Magnetic Resonance 158 (2002) 126–142.
[6] A.V. Astashkin, A.M. Raitsimring, Electron spin echo envelope modulation theory for high electron spin systems in weak crystal field, Journal of Chemical Physics 117 (2002) 6121–6132.
[7] R.G. Larsen, C.J. Halkides, D.J. Singel, A geometric representation of nuclear modulation effects—the effects of high electron-spin multiplicity on the electron-spin echo envelope modulation spectra of Mn-2+ complexes of N-Ras P21, Journal of Chemical Physics 98 (1993) 6704–6721.
[8] A.R. Coffino, J. Peisach, Nuclear modulation effects in high-spin electron-systems with small zero-field splittings, Journal of Chemical Physics 97 (1992) 3072–3091.
[9] C. Buy, G. Girault, J.L. Zimmermann, Metal binding sites of H+-ATPase from chloroplast and Bacillus PS3 studied by EPR and pulsed EPR spectroscopy of bound manganese(II), Biochemistry 35 (1996) 9880–9891.
[10] C.G. Hoogstraten, C.V. Grant, T.E. Horton, V.J. DeRose, R.D. Britt, Structural analysis of metal ion ligation to nucleotides and

nucleic acids using pulsed EPR spectroscopy, Journal of the American Chemical Society 124 (2002) 834–842.
[11] P. Manikandan, R. Carmieli, T. Shane, A.J. Kalb, D. Goldfarb, W-band ENDOR investigation of the manganese-binding site of concanavalin A: determination of proton hyperfine couplings and their signs, Journal of the American Chemical Society 122 (2000) 3488–3494.
[12] O. Schiemann, J. Fritscher, N. Kisseleva, S.T. Sigurdsson, T.F. Prisner, Structural investigation of a high-affinity Mn-II binding site in the hammerhead ribozyme by EPR spectroscopy and DFT calculations. Effects of neomycin B on metal-ion binding, Chembiochem 4 (2003) 1057–1065.
[13] B. Schneider, C. Sigalat, T. Amano, J.L. Zimmermann, Evidence for changes in the nucleotide conformation in the active site of H+-ATPase as determined by pulsed EPR spectroscopy, Biochemistry 39 (2000) 15500–15512.
[14] C.J. Walsby, J. Telser, R.E. Rigsby, R.N. Armstrong, B.M. Hoffman, Enzyme control of small-molecule coordination in FosA as revealed by P-31 pulsed ENDOR and ESE-EPR, Journal of the American Chemical Society 127 (2005) 8310–8319.
[15] A. Zoleo, S. Contessi, G. Lippe, L. Pinato, M. Brustolon, L.C. Brunel, F. Dabbeni-Sala, A.L. Maniero, High-affinity metal-binding site in beef heart mitochondrial F(1)ATPase: An EPR spectroscopy study, Biochemistry 43 (2004) 13214–13224.
[16] R.G. Larsen, C.J. Halkides, A.G. Redfield, D.J. Singel, Electron-spin echo envelope modulation spectroscopy of Mn-2+.Gdp complexes of N-Ras P21 with selective N-15 labeling, Journal of the American Chemical Society 114 (1992) 9608–9611.
[17] C.J. Halkides, C.T. Farrar, R.G. Larsen, A.G. Redfield, D.J. Singel, Characterization of the active-site of P21 Ras by electron-spin echo envelope modulation spectroscopy with selective labeling—comparisons between Gdp and Gtp forms, Biochemistry 33 (1994) 4019–4035.
[18] C.J. Halkides, B.F. Bellew, G.J. Gerfen, C.T. Farrar, P.H. Carter, B. Ruo, D.A. Evans, R.G. Griffin, D.J. Singel, High frequency (139.5 GHz) electron paramagnetic resonance spectroscopy of the GTP form of p21 ras with selective O-17 labeling of threonine, Biochemistry 35 (1996) 12194–12200.
[19] C.T. Farrar, C.J. Halkides, D.J. Singel, The frozen solution structure of p21 ras determined by ESEEM spectroscopy reveals weak coordination of Thr35 to the active site metal ion, Structure 5 (1997) 1055–1066.
[20] R. LoBrutto, G.W. Smithers, G.H. Reed, W.H. Orme-Johnson, S.L. Tan, J.S. Leigh, Observation of Manganese(II)-ligand superhyperfine couplings in complexes with proteins by electron spin-echo spectroscopy, Biochemistry 25 (1986) 5654–5660.
[21] J. McCracken, J. Peisach, L. Bhattacharyya, F. Brewer, Electron-spin echo envelope modulation studies of lectins—evidence for a conserved Mn2+-binding site, Biochemistry 30 (1991) 4486–4491.
[22] M.P. Espe, J.P. Hosler, S. Ferguson-Miller, G.T. Babcock, J. McCracken, A continuous-wave and pulsed Epr characterization of the Mn^{2+} binding-site in Rhodobacter-Sphaeroides cytochrome-C-oxidase, Biochemistry 34 (1995) 7593–7602.
[23] J.E. Wertz, J.R. Bolton, Electron Spin Resonance: Elementary Theory and Practical Applications, Chapman and Hall, New York, 1986.
[24] B. Bleaney, D.J.E. Ingram, The paramagnetic resonance spectra of 2 salts of manganese, Proceedings of the Royal Society of London Series a-Mathematical and Physical Sciences 205 (1951) 336–356.
[25] R.d.L. Kronig, C.J. Bouwkamp, Spin-levels and paramagnetic dispersion in iron-ammoniumalum, Physica 6 (1939) 290–298.
[26] B. Bleaney, R.S. Trenam, Paramagnetic resonance spectra of some ferric alums the nuclear magnetic moment of Fe-57, Proceedings of the Royal Society of London Series a-Mathematical and Physical Sciences 223 (1954) 1–14.
[27] C. Sandmark, C.I. Branden, Crystal structure of hexaimidazole zinc]2) dichloride tetrahydrate Zn(C3H4N2)6Cl2.4H20, Acta Chemica Scandinavica 21 (1967) 993.
[28] T.P.J. Garrett, J.M. Guss, H.C. Freeman, Hexakis(Imidazole)Manganese(II) Dichloride Tetrahydrate, [Mn(C3H4N2)6]Cl2.4H2O, and Hexakis(Imidazole)Zinc(II) Dichloride Tetrahydrate, [Zn(C3H4N2)6]Cl2.4H2O, Acta Crystallographica Section C-Crystal Structure Communications 39 (1983) 1027–1031.
[29] A. Schweiger. in L. Kevan, M.K. Bowman (Eds.), Modern Pulsed and Continuous-Wave Electron Spin Resonance, Wiley, New York, 1990.
[30] P.S. Rao, S. Subramanian, Single-crystal electron-paramagnetic-Res studies of some 1st-row transition ions in hexaimidazole zinc(II)dichloride tetrahydrate. 4. Mn(II)—a case of twinning, Molecular Physics 54 (1985) 429–438.
[31] G.M. Woltermann, J.R. Wasson, Electron-spin resonance study of Hexakis(pyridine *N*-oxide)manganese(II) perchlorate complexes, Inorganic Chemistry 12 (1973) 2366–2370.
[32] R. Hrabanski, electron-paramagnetic resonance of Mn(II) in [M(H2O)6]Ptcl6 (M = Zn, Mg, Cd) single-crystals, Spectrochimica Acta Part A-Molecular and Biomolecular Spectroscopy 48 (1992) 631–637.
[33] B.P. Maurya, A. Punnoose, M. Ikram, R.J. Singh, Epr Study of Mn2+ ion doped in potassium oxalate monoperhydrate single-crystal, Polyhedron 14 (1995) 2561–2567.
[34] B.N. Figgis, M.A. Hitchman, Ligand Field Theory and its Applications, Wiley-VCH, New York, 2000.
[35] C.I.H. Ashby, C.P. Cheng, T.L. Brown, N-14 nuclear-quadrupole resonance-spectra of coordinated imidazole, Journal of the American Chemical Society 100 (1978) 6057–6063.
[36] C.P. Scholes, A. Lapidot, R. Mascarenhas, T. Inubushi, R.A. Isaacson, G. Feher, Electron nuclear double-resonance (Endor) from heme and histidine nitrogens in single-crystals of aquometmyoglobin, Journal of the American Chemical Society 104 (1982) 2724–2735.
[37] I. Gromov, J. Shane, J. Forrer, R. Rakhmatoullin, Y. Rozentzwaig, A. Schweiger, A Q-band pulse EPR/ENDOR spectrometer and the implementation of advanced one- and two-dimensional pulse EPR methodology, Journal of Magnetic Resonance 149 (2001) 196–203.
[38] I. Gromov, J. Forrer, A. Schweiger, Probehead operating at 35 Ghz for continous wave and pulse electron paramagnetic resonance applications, Review of Scientific Instruments 77 (2006) 064704.
[39] A. Schweiger, G. Jeschke, Principles of pulse electron paramagnetic resonance, Oxford University Press, Oxford, 2001.